Brain Tumor Classification from Radiology and Histopathology using Deep Features and Graph Convolutional Network

Arijit De*, Radhika Mhatre†, Mona Tiwari‡, Ananda S. Chowdhury*

*Department of Electronics and Telecommunication Engineering, Jadavpur University, Kolkata, West Bengal, India
Email: as.chowdhury@jadavpuruniversity.in
†Unipath Specialty Laboratory Ltd., Ahmedabad, Gujrat, India
‡Department of Neuro-Radiology, Institute of Neurosciences, Kolkata, West Bengal, India

Abstract—In this paper, we address the problem of brain tumor classification from radiology and histopathology data. A coarse-to-fine classification approach is adopted using a combination of deep features and Graph Convolution Network (GCN). As a first coarse step, we use 3D CNN to detect Glioblastoma from MRI images. In order to infer about Astrocytoma and Oligodendroglioma, Whole Slide Images (WSI) are employed in the second stage. During this fine classification stage, 2D CNN features are extracted at two different (global and local) magnification levels. A graph is constructed with nodes in the space of concatenated global and local features. Edges are constructed from feature similarity and graph topology. Finally, GCN is used with normalized graph Laplacian to ensure better relation-aware-representation leading to more accurate classification. Experimental comparisons on the CPM-RadPath2020 challenge dataset clearly demonstrate the state-of-the-art performance of our proposed strategy. The code implementation is available at https://github.com/arijitde92/BrainTumorClassification.

Index Terms - Brain tumor classification, MRI, WSI, Graph Convolution Network.

I. INTRODUCTION

Gliomas are the most frequently occurring primary malignant tumors of the central nervous system (CNS). Every year approximately 100,000 new cases, diagnosed with Gliomas are reported [1]. Although Magnetic Resonance Imaging (MRI) is widely used to study the tumour and prepare treatment plans, it cannot provide detailed depiction of gliomas (e.g. grading and sub-typing) as the tumour micro-environment is quite complex and spatial heterogeneity is not well reflected in MRI. Thus, along with MRI, histopathology examination is often pre-scribed [2]. In histopathology, glial cells exhibit morphological characteristics like increase in cellularity, necrosis in tumour region, vascular proliferation, and degeneration of normal brain parenchyma due to tumour cell invasion. Availability of such information makes histopathological data more amenable for detailed classification of the gliomas [3], [4]. Histopatho-logical classification of brain tumours is dependent on the recognition of areas with the characteristic histopathology for a particular tumour type. Classification of gliomas into astro-cytoma, oligodendroglioma and glioblastoma is the foundation upon which relies the prognosis, treatment and management of the patient. Microscopic examination remains the gold standard. However, there is great inter-observer variability based on the subjective evaluation. Use of machine learning algorithms utilising the particular histopathological character-istics of individual tumours, independent of subjective analysis can help reduce this diagnostic variability. With advances in digital pathology and whole slide imaging, morphology based automated pathologic diagnosis has become a reality.

The Computational Precision Medicine Radiology-pathology challenge [5] opened the path for independent researchers to develop classification techniques using their publicly available dataset containing Whole Slide Images (WSI) and MRIs in pairs. Sahayam et al. [6] used only radiology data to perform classification which resulted in lower classification accuracy. Chan et al. [7] applied a random forest into clusters of WSI tiles grouped together using unsupervised methods to classify gliomas. Xue et al. and Pei et al. [8], [9] undertook tumor segmentation followed by tumor classification on MRI volumes. The three-way simultaneous classification yielded lower accuracy than binary classification. Hamidinekoo et al. [10] also used three-way simultaneous classification and applied 2D CNN for both radiology and histopathology data. 2D CNN used for slice-wise classification in 3D MRI volumes is inefficient as 3D CNN captures more spatial information. Bagari et al. [11] employed a soft-voting ensemble using both radiological and histopathological data. The radiological model exploits radiomics from MRI data and the histopathological model uses patches extracted from WSIs filtered by an outlier detection algorithm. So far, their classification technique is the top-performing method. The second-best approach [12] also used both MRI and WSI to create two separate models. An end-to-end deep learning approach is used to classify the radiological data, while the histopathological model uses deep feature extraction from WSI data, to further classify a set of extracted tiles. Ma et al. [13] used 3D DenseNet followed by a regression model for classifying radiological data. For classifying histopathological data, ResNet34 and ResNet50 were directly applied to extract features from WSI patches. Pei et al. [14] used only radiological data to segment the

4420

tumor region and then classified it using a regular 3D CNN model. They did not use the enormous information that could be exploited from WSI.

In this paper, we propose a coarse-to-fine approach for multi-modal tumor classification into glioblastoma, astrocytoma and oligodendroglioma using radiological as well as histopathological images. Our main contributions are listed below:

1) We apply a 3D CNN model for a coarse classification, i.e. glioblastoma vs. non-glioblastoma (which could be either astrocytoma or oligodendroglioma) from 3D MRI volumes.

2) We construct a deep feature extraction model for WSI using 2D CNN. Features from two different magnification levels of the WSI are treated as local and global features.

3) We employ Graph Convolutional Network (GCN) for fine classification of non-glioblastoma into astrocytoma and oligodendroglioma. A feature vector combining the local and global features is used as a node. Edges are constructed by considering both feature similarity and graph topology.

II. PROPOSED METHOD

Our proposed method primarily performs a coarse to fine classification consisting of three major steps, namely, i) radiological data classification, ii) histopathological feature extraction and iii) classification of histopathological data using GCN. The overall flowchart of our classification technique is portrayed in Fig.1. We first perform a coarse classification from the radiological data by inferring presence or absence of Glioblastoma. This is possible as Glioblastoma exhibit distinctive macro features which can be identified from the MRI data. However, 3D MRI volumes provide very little information about tumor subtypes like oligodendroglioma and astrocytoma. Fig. 2 demonstrates how Glioblastoma can be identified radiologically but due to the lack of distinctive radiological features in oligodendroglioma and astrocytoma, they are difficult to be identified. So, we use histopathological data for subsequent finer classification.

A. Radiological phase

In this step, we consider only radiological data, i.e., 3D MRI volumes. Each subject has 4 different types of MRI, namely, t1, t2, t1ce, and flair. We perform binary classification by dividing the data into two groups for each MRI type, one group consists of only glioblastoma subjects and the other group consists of astrocytoma and oligodendroglioma subjects.

1) Data pre-processing: Each MRI volume is first corrected using the N4 bias field correction algorithm [15], which is widely used for correcting non-uniformity present in the MRI data due to low frequency intensities. The original resolution of each corrected volume was $240 \times 240 \times 155$. Due to memory constraints, this volume was down-sampled to a resolution of $128 \times 128 \times 128$ using cubic interpolation re-sampling algorithm from SimpleITK library [16].
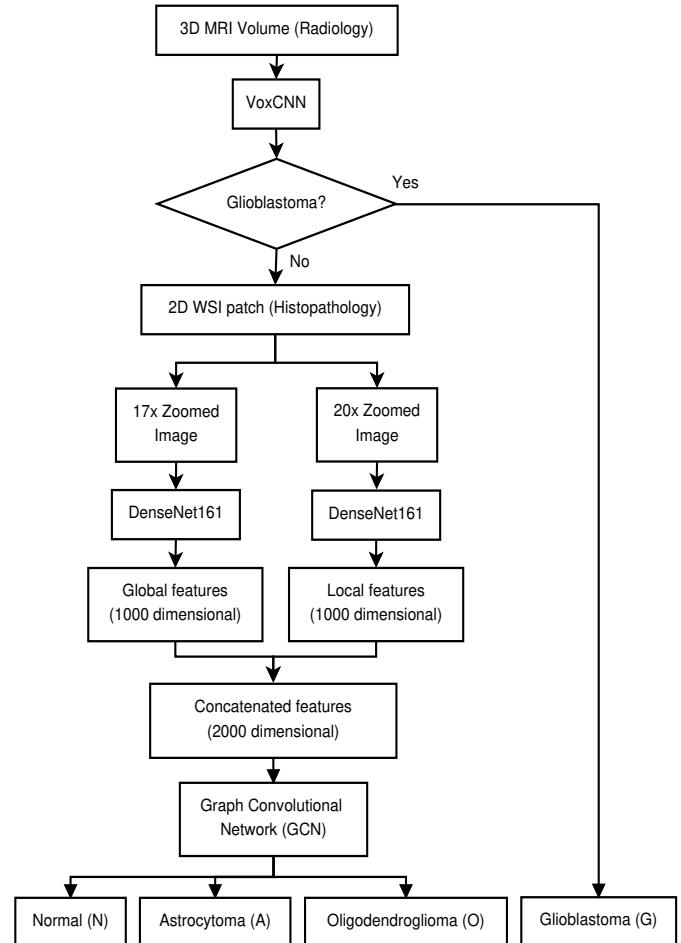
Fig. 1: Flowchart of our classification model.

2) Data augmentation: Since, the number of subjects belonging to each class is different we apply horizontal flipping along the sagittal plane on the volumes belonging to minority class to balance the samples of each class.

3) Classification model: The classification was based on VoxCNN [17] with appropriate modifications. In this case, VoxCNN is trained from scratch for each of the four MRI types separately. Modulated rank averaging method is applied next to perform weighted voting among the 4 MRI types to arrive at the final prediction.

B. Histopathological phase

Patch selection for training the model is a very important task as discriminative, noise-free patches will help the model learn properly. The process is often time consuming and prone to errors. Weakly-supervised approaches [18] only use the slide labels during the training of the aggregation model. In contrast, we adopted a semi-automated approach for optimal selection of tiles.

1) Patch selection: To select the most important tiles to classify WSIs, we have adopted a two-stage approach.
Stage 1: We extract tiles/patches of size 1000×1000 pixels without any overlaps from each WSI using deep zoom ex-
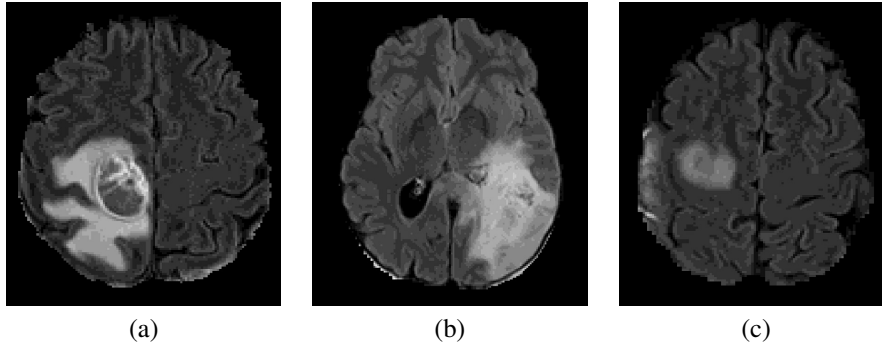
Fig. 2: Axial flair MRI images of (a) Glioblastoma Multiforme, (b) Astrocytoma, (c) Oligodendroglioma. It can be seen in case of (a) the tumor region has thick demarcations with a central dark necrotic region and an irregular whitish edema region while in cases of (b) and (c) there is no such distinctive feature

tractor provided in the openslide framework [19]. Each WSI produces patches from different magnification levels. We select two such levels for our work. The first one has the highest level of magnification (20x) representing the local features and the other is 3 times zoomed out (17x), representing the global features. After experimentation, we found selecting two such levels give the best representation of each WSI.

Stage 2: The histopathology images contain patches that include air bubbles, cracks, and blurred regions. We remove those tiles by studying the histogram of the images. For this purpose, we devised an automated technique selecting only those images that have a balanced histogram, i.e., those images that have higher number of pixels between intensity range 0 - 192 than those in the range 192 - 255 in all three color channels. After careful observations, we found that the artifacts mentioned above are mostly grayscale and hence have most of the pixels with intensity greater than 192 in all three channels. Here the lowest intensity 0 represents white and highest intensity 255 represents black.

Stage 3: Even after removing unnecessary patches, some of them do not contain the necessary cellular information as the tumor has not spread through out the whole tissue scanned in the laboratory. Some regions had healthy cells while others had tumor cells distinctly visible. Our neuro-pathologists manually select patches that contain only healthy cells labelled as 'N' (normal) and patches that contain more than 80% tumor cells, labelled as 'A' (astrocytoma) or 'O' (oligodendroglioma). Example images of normal, glioblastoma, astrocytoma and oligodendroglioma at two different magnification levels are shown in Fig. 3. We have selected equal number of patches for each class from each magnification level to prevent class imbalance. The extracted tiles were visually inspected randomly to ensure that the training set is free of false tiles.

2) Deep feature extraction: We apply DenseNet model [20] with 161 layers to extract the deep features from each patch. We chose DenseNet over other popular neural networks like VGGNet or ResNet because DenseNet is more complex than VGGNet and achieves better results using fewer parameters than ResNet. The last two layers of DenseNet are modified to

extract features of 1000 dimensions. The model is trained to classify among three classes ('A', 'O' and 'N'). Let the feature vector F_i for an image i ($i = 1, \cdots, M$) be represented as:

$$F_i = [F_{gi}^{(1)}, \cdots, F_{gi}^{(1000)}, F_{li}^{(1)}, \cdots, F_{li}^{(1000)}] \qquad (1)$$

$$F_{gi}^{(j)} = \frac{\sum_{x=1}^{S} F_{gx}^{(j)}}{S}, j = 1, \cdots, 1000; x \in i \qquad (2)$$

and

$$F_{li}^{(j)} = \frac{\sum_{x=1}^{T} F_{lx}^{(j)}}{T}, j = 1, \cdots, 1000; x \in i \qquad (3)$$

Here, $F_i = [F_i^{(j)}, j = 1, \cdots, d_f]$ ($d_f = 2000$) is obtained by concatenating 1000 dimensional global feature vector $F_{gi} = [F_{gi}^{(j)}, j = 1, \cdots, 1000]$ and the 1000 dimensional local feature vector $F_{li} = [F_{li}^{(j)}, j = 1, \cdots, 1000]$. Total number of patches (x denotes a patch) at the global level is denoted by S and that at the local level is denoted by T. For this work, $S = 150$ and $T = 1000$. For each component of the global and local feature vector, averaging is done over all the patches.

C. Graph Convolutional Network

To achieve more precise and accurate classification, graph convolutional network (GCN) is employed which can effectively capture the relation-aware representation (RAR). Most of the classification models provide attractive results when provided with a huge set of labeled samples. However, GCN can perform well with fewer training samples, which is the case for the present problem. RAR can provide the necessary information to guide the training with fewer examples. GCN can help generalize the standard convolution operation to graph convolution [21].

1) Graph Construction: We construct a graph $G = G(V, E)$, with M nodes $v_i \in V, i = 1, \cdots, M$ and a number of edges $e_{ij} = (v_i, v_j) \in E$. Here each node v_i is represented by the concatenated feature vector F_i and M denotes the number of image samples in training set. The adjacency matrix A defines the relationships (or edges) between the vertices. We construct edges between nodes by considering the feature similarity of the nodes as well as by respecting graph topology. Such constructions make the graph informative and sparse leading to better accuracy with high computational efficiency.

4422
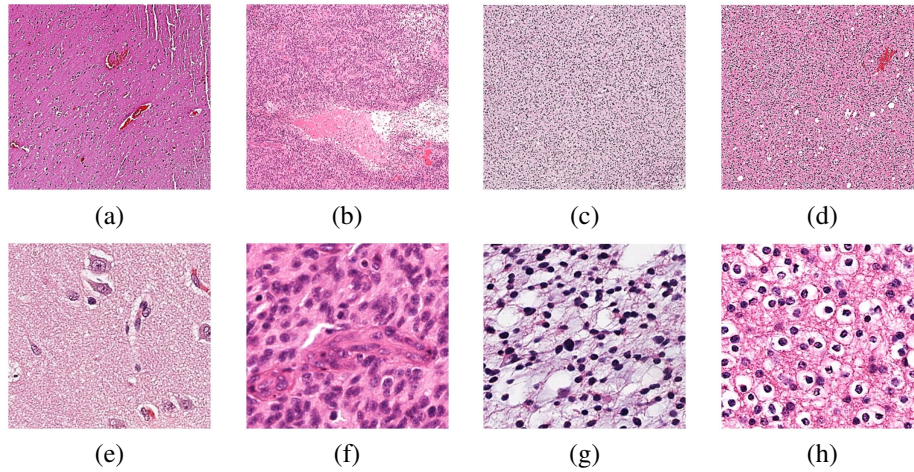
Fig. 3: Histopathology images of (a) normal, (b) glioblastoma, (c) astrocytoma and (d) oligodendroglioma cells with global magnification level (20x). Corresponding images (e), (f), (g) & (h) are shown with local magnification level (17x).

Feature similarity between two nodes v_i and v_j is captured by employing a RBF kernel $R_{i,j}$ in the following manner:

$$R_{i,j} = \begin{cases} 1 & \text{if } \exp\left(-\frac{\|v_i - v_j\|^2}{\delta^2}\right) > \lambda \\ 0 & \text{otherwise} \end{cases} \quad (4)$$

Here, δ is a parameter which controls the width of the RBF kernel and λ is the similarity threshold. Both the parameters, δ and λ are set experimentally.

We next set edge connections from graph topology by analyzing the nature of labelled nodes within a certain neighborhood of an unlabelled node (20 % of the total vertices are unlabelled). The kNN algorithm is applied to obtain k neighbors with $k = \sqrt{M}$. Let, $N_k(v_i)$ denotes the set of k neighbors for the node v_i. Further, let $N_k^{(c)}(v_i)$ denote the set of neighbors having class label c within its k neighbors. We then compute the probability of the node v_i to belong to a class c as $p(v_i^{(c)}) = |N_k^{(c)}(v_i)|/|N_k(v_i)|$. Here, $c = 1$ denotes Astrocytoma class, $c = 2$ denotes Oligodendroglioma class and $c = 3$ denotes Normal class. We now formulate the following three conditions:

1) Two labelled nodes are connected only if they belong to the same class.
2) An unlabelled node v_i is connected to a labelled node v_j if the probability of v_i to belong to the class c of v_j exceeds a certain threshold. So, e_{ij} maybe constructed if $v_j \in c$ and $p(v_i^{(c)}) > \zeta$, where, ζ is an experimentally chosen threshold and $c = 1, 2, 3$.
3) Two unlabelled nodes v_i and v_j are connected if both of them have similar affinities to belong to the different classes. We compute the difference of probabilities of these two nodes to belong to the three different classes and examine if the maximum of these differences falls below a certain threshold. Therefore, e_{ij} maybe constructed if $max(|p(v_i^{(c)}) - p(v_j^{(c)})|) < \omega$ with $c = 1, 2, 3$. We set the threshold ω experimentally.

Thus, the spatial connectivity between any two nodes v_i and v_j can be represented as:

$$S_{i,j} = \begin{cases} 1 & \text{if condition (1) or (2) or (3) is met} \\ 0 & \text{otherwise} \end{cases} \quad (5)$$

Now, to construct the adjacency matrix A, each element in A is computed in the following way:

$$A_{i,j} = \begin{cases} 1 & \text{if } R_{i,j} = 1 \text{ and } S_{i,j} = 1 \\ 0 & \text{otherwise} \end{cases} \quad (6)$$

We next obtain the graph Laplacian matrix L as follows:

$$L = D - A \quad (7)$$

where D is a diagonal matrix representing the degrees of A, i.e., $D_{i,i} = \sum_j A_{i,j}$. GCNs make use of the eigen-decomposition of graph Laplacian matrix to implement information propagation within graph [21]. The symmetric normalized Laplacian matrix (L_{sym}) is used as shown below to amplify the generalization ability of the graph.

$$\begin{aligned} L_{sym} &= D^{-\frac{1}{2}} L D^{-\frac{1}{2}} \\ &= I - D^{-\frac{1}{2}} A D^{-\frac{1}{2}} \end{aligned} \quad (8)$$

where I is the identity matrix. Thus, GCN is able to apprehend the RAR feature [22].

2) Graph Convolutional Layers: GCN is used primarily to express G through a neural network model $f(X, A)$ in which $X \in R^{N \times d_f}$. Mathematically, all feature representation for all nodes are updated by a multi-layer GCN via the layer-wise rule:

$$H^{(l+1)} = \sigma(L_{sym} H^{(l)} W^{(l)}) \quad (9)$$

where σ is the ReLU function. $H^{(l)} \in R^{N \times d_l}$ stands for the feature representation of lth layer. Considering $X = H^{(0)}$, a two-layer GCN (2L-GCN) has the following layers:

$$H^{(1)} = \sigma(L_{sym} \times W^{(0)}) \quad (10)$$

$$H^{(2)} = \sigma(L_{sym} H^{(1)} W^{(1)}) \quad (11)$$

4423

where, $W^{(0)} \in R^{d_0 \times d_1}$ and $W(1) \in R^{d_1 \times d_2}$ are two trainable weight matrices. The node feature set V and the adjacency matrix A are passed to a 2L-GCN to obtain $H^{(2)} \in R^{N \times D}$ where $D = d_f$. Then, a dot product of $H^{(2)}$ and I is computed as given by:

$$y = H^{(2)}I \qquad (12)$$

Finally, through a linear projection (LP) with trainable weights $W^{(2)} \in R^{N \times N_C}$, we obtain:

$$z = yW^{(2)} + W^b \qquad (13)$$

Here $z \in R^{N_C}$, N_c is the number of classes and W^b represents the bias. For this problem $N_C = 3$. Note that only $(W^{(0)}, W^{(1)}, W^{(2)})$ and linked biases needs to be trained for this two layered GCN. We use a cross entropy loss for three classes to train the network and update the parameters.

III. EXPERIMENTAL RESULTS

A. Dataset

To train and validate our pipeline, we used the CPM-RadPath 2020 challenge dataset [23]. The dataset consists of multi-institutional paired MRI scans and WSIs of brain gliomas, obtained from the same patients. Each subject, belongs to one of the following class- 'A' (astrocytoma), 'O' (Oligodendroglioma) and 'G' (Glioblastoma). The dataset contains 255 co-registered radiology and histopathology subjects respectively split into 221 samples in training set and remaining 34 in testing set. The radiology data consists of four modalities: t1, t2, t1ce, and flair. The data is distributed after pre-processing, co-registering to the same anatomical template, interpolating to the same resolution ($1mm^3$), and skull-stripping of each and every subject. The histopathology data consists of one WSI for each subject, captured from H&E stained tissue specimens.

B. Training VoxCNN, DenseNet and GCN

All the computations are done in HP Z640 Workstation with Intel Xeon 14-core Processor having 128GB Random Access Memory (RAM) and NVIDIA Titan RTX 24GB Graphics processor using PyTorch 1.9 [24] and PyTorch Geometric [25] in Ubuntu 20.04. For the radiological classification (Section II-A3), the batch size, learning rate and total number of epochs are 16, 27×10^{-6} and 200 respectively. For the histopatholgy image classification (Section II-B2), each image was resized to 224×224 as required by the DenseNet model. The batch size, learning rate and total number of epochs are 32, 3×10^{-7} and 300 respectively. For the construction of the adjacency matrix required to train GCN (Section II-C1), the δ, λ, ω and ζ parameters are experimentally set to 5, 0.75, 0.1 and 0.6 respectively. The GCN is trained for 1200 epochs with a learning rate of 3×10^{-4}. Adam optimizer and cross entropy loss function are used for 3D CNN, 2D CNN and GCN. The implemented code is available for reproducibility at https://github.com/arijitde92/BrainTumorClassification.

TABLE I: Optimal Magnification Levels for Global and Local Features

Combination	Accuracy (%)
15x and 20x	87.3
13x and 17x	81.7
17x and 20x	**91.4**

TABLE II: Impact of ω on Classification Accuracy

ω	Accuracy (%)
0.1	**91.4**
0.15	90.7
0.2	90.2
0.25	89.6
0.3	88.3
0.4	87.5
0.5	85.2

C. Optimal Parameter Setting

We first show in table I that using 2D histopatholgy images with magnification levels of 17x and 20x achieves optimal classification accuracy as compared to using other combinations of 15x & 20x and 13x & 17x. We next demonstrate through Fig. 4, that optimal values of λ and δ, used in edge building with RBF kernel are 0.75 and 3 respectively. Finally, optimal values of the parameters ζ and ω, used for edge construction from graph topology are determined. Tables II and III respectively show the optimal values of ω and ζ to be 0.1 and 0.6 respectively.

D. Ablation Studies

We have conducted two ablation studies. The first ablation study reveals the impacts of individual modalities, *i.e.*, radiology and histopathology. As can be seen from Table IV the proposed model which combines 3D MRI and 2D WSI data achieves the highest accuracy compared to 3D MRI and 2D WSI applied in isolation. In the second ablation study, we compare the individual impacts of the two different edge building approaches (as proposed in Sec II-C1) and show the performance to be best when both feature similarity and graph topology are combined together. The results are included in Table V. We have also tested the potential of the MRI component of our solution for a 2-class brain tumor classification task as a recent work reported similar classification results in 2D on a different dataset [26]. We achieve an accuracy of 88.57% whch is slightly higher than the accuracy of 88% as reported in [26].

E. Comparisons with Deep Baseline Models

Keeping the workflow structure same as shown in Fig. 1, we ran our experiments with some deep baseline models like

TABLE III: Impact of ζ on Classification Accuracy

ζ	Accuracy (%)
0.3	87.23
0.4	88.76
0.5	90.37
0.6	**91.4**
0.7	89.53
0.8	86.5

4424
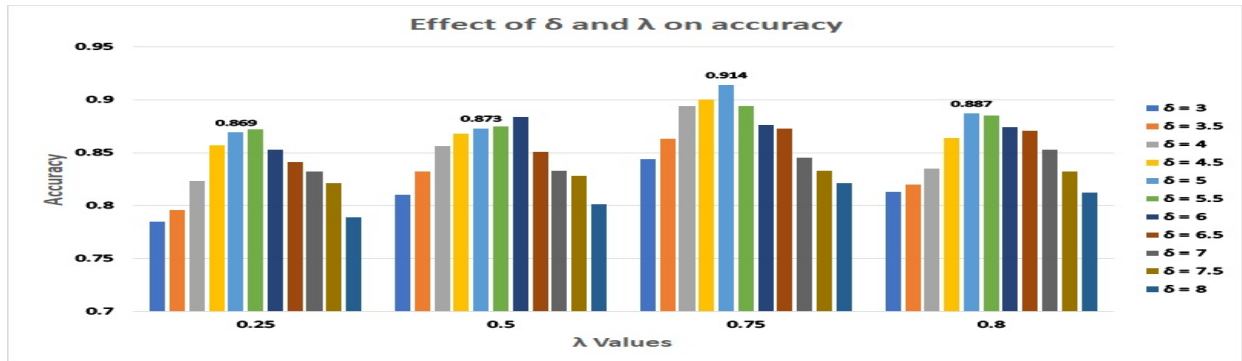
Fig. 4: Impact of δ and λ on classification accuracy

TABLE IV: Ablation Study I: Impact of MRI and WSI

Approach	F1 Score	Cohen's Kappa	Balanced Accuracy
MRI Only	0.668	0.632	0.76
WSI Only	0.812	0.787	0.86
MRI+WSI	**0.914**	**0.871**	**0.914**

TABLE V: Ablation Study II: Impact of Feature Similarity and Graph Topology for Edge Construction

Approach	F1 Score	Cohen's Kappa	Balanced Accuracy
Feature Similarity only	0.903	0.862	0.904
Graph Topology only	0.885	0.826	0.886
Both	**0.914**	**0.871**	**0.914**

ResNet [27], DenseNet [20] and MobileNet V3 [28]. For predictions on the test set, we first used radiology (MRI) data to determine the Glioblastoma cases using modulated rank averaging technique used in [17]. We then used the histopathology (WSI) data of the non-Glioblastoma cases to classify among Astrocytoma and Oligodendroglioma along with Normal (healthy) images. For the sake of comparison, we replaced both VoxCNN and GCN first with ResNet, then with DenseNet, and finally with MobileNet V3. As can be seen from Table VI, performances of all the three baseline deep networks are found to be quite inferior as compared to our method. This is mainly because VoxCNN is able to learn better features than these deep networks while classifying radiology data. Furthermore, an informative graph constructed using feature similarity as well as graph topology has resulted in better classification accuracy.

F. Comparisons with State-of-the-Art Approaches

We now show comparisons with eight state-of-the-art models in Table VII. Like other reported works, we have evaluated

TABLE VI: Comparison with Deep Baseline Models

Approach	F1 Score	Cohen's Kappa	Balanced Accuracy
ResNet50	0.794	0.652	0.82
DenseNet169	0.794	0.665	0.835
MobileNet V3	0.705	0.491	0.702
Ours	**0.914**	**0.871**	**0.914**

TABLE VII: Comparison with State Of The Art Models

Models	F1 Score	Cohen's Kappa	Balanced Accuracy
Sahayam et al. [6]	-	-	0.754
Chan et al. [7]	-	-	0.78
Xue et al. [8]	-	-	0.849
Pei et al. [9]	0.886	0.801	0.8
Momemi et al. [12]	-	-	0.85
Hamidinekoo et al. [10]	0.886	0.811	0.860
Wang et al. [29]	**0.943**	**0.903**	0.889
Bagari et al. [11]	-	-	0.9
Ours	0.914	0.871	**0.914**

our model using three different metrics, namely, F1-Score (micro averaged), Cohen's Kappa and Balanced Accuracy. As the results demonstrate, we have clearly surpassed [6], [7], [8], [9], [10] in terms of all the three measures. We have outperformed [29] in terms of the balanced accuracy but have marginally lost in terms of F1 score and Cohen's Kappa. Further, our method yielded superior results than both the best [11] and the second best [12] teams on the CPM RadPath Challenge [5].

IV. CONCLUSION

In this paper, we have addressed the problem of multi-class classification of brain tumors using both MRI and histopathology data using a coarse-to-fine approach. We employed VoxCNN for MRI based coarse classification of the gliomas into Glioblastoma and non-Glioblastoma. Graph convolutional network is employed for fine classification of non-Glioblastoma into Astrocytoma and Oligodendroglioma along with normal (healthy) class from the histopathology data. We demonstrated how a better graph for GCN built using feature similarity and graph topology can yield accurate results. Experimental comparisons clearly reveal that our proposed model could achieve state-of-the-art performance. In future, other modalities and tumor grades will be included to perform a more comprehensive classification.

V. ACKNOWLEDGEMENT

REFERENCES

[1] F. Bray *et al.*, "Global cancer statistics 2018: Globocan estimates of incidence and mortality worldwide for 36 cancers in 185 countries," *CA: A Cancer Journal for Clinicians*, vol. 68, no. 6, pp. 394–424, 2018.

[2] F. G. Dhermain, P. Hau, H. Lanfermann, A. H. Jacobs, and M. J. van den Bent, "Advanced mri and pet imaging for assessment of treatment response in patients with gliomas," *The Lancet Neurology*, vol. 9, no. 9, pp. 906–920, 2010.

[3] V. Kumar, A. K. Abbas, and J. C. Aster, *Robbins basic pathology e-book*. Elsevier Health Sciences, 2017.

[4] Z. Ye, R. L. Price, X. Liu, J. Lin, Q. Yang, P. Sun, A. T. Wu, L. Wang, R. H. Han, C. Song *et al.*, "Diffusion histology imaging combining diffusion basis spectrum imaging (dbsi) and machine learning improves detection and classification of glioblastoma pathology," *Clinical Cancer Research*, vol. 26, no. 20, pp. 5388–5399, 2020.

[5] T. Kurc *et al.*, "Segmentation and classification in digital pathology for glioma research: challenges and deep learning approaches," *Frontiers in Neuroscience*, vol. 14, p. 27, 2020.

[6] S. Sahayam, U. Jayaraman, and B. Teja, "Multi-class glioma classification from mri images using 3d convolutional neural networks," in *International Conference on Computer Vision and Image Processing*. Springer, 2020, pp. 327–337.

[7] H.-W. Chan, Y.-T. Weng, and T.-Y. Huang, "Automatic classification of brain tumor types with the mri scans and histopathology images," in *International MICCAI Brainlesion Workshop*. Springer, 2019, pp. 353–359.

[8] Y. Xue *et al.*, "Brain tumor classification with tumor segmentations and a dual path residual convolutional neural network from mri and pathology images," in *International MICCAI Brainlesion Workshop*. Springer, 2019, pp. 360–367.

[9] L. Pei *et al.*, "A hybrid convolutional neural network based-method for brain tumor classification using mmri and wsi," in *International MICCAI Brainlesion Workshop*. Springer, 2020, pp. 487–496.

[10] A. Hamidinekoo, T. Pieciak, M. Afzali, O. Akanyeti, and Y. Yuan, "Glioma classification using multimodal radiology and histology data," in *International MICCAI Brainlesion Workshop*, 2020.

[11] A. Bagari, A. Kumar, A. Kori, M. Khened, and G. Krishnamurthi, "A combined radio-histological approach for classification of low grade gliomas," in *International MICCAI Brainlesion Workshop*. Springer, 2018, pp. 416–427.

[12] A. Momeni, M. Thibault, and O. Gevaert, "Dropout-enabled ensemble learning for multi-scale biomedical data," in *International MICCAI Brainlesion Workshop*. Springer, 2018, pp. 407–415.

[13] X. Ma and F. Jia, "Brain tumor classification with multimodal mr and pathology images," in *International MICCAI Brainlesion Workshop*. Springer, 2019, pp. 343–352.

[14] L. Pei *et al.*, "Brain tumor classification using 3d convolutional neural network," in *International MICCAI brainlesion workshop*. Springer, 2019, pp. 335–342.

[15] N. J. Tustison, B. B. Avants, P. A. Cook, Y. Zheng, A. Egan, P. A. Yushkevich, and J. C. Gee, "N4itk: improved n3 bias correction," *IEEE Trans. Med. Imag*, vol. 29, no. 6, pp. 1310–1320, 2010.

[16] Z. Yaniv, B. C. Lowekamp, H. J. Johnson, and R. Beare, "Simpleitk image-analysis notebooks: a collaborative environment for education and reproducible research," *Journal of Digital Imaging*, vol. 31, no. 3, pp. 290–303, 2018.

[17] A. De and A. S. Chowdhury, "Dti based alzheimer's disease classification with rank modulated fusion of cnns and random forest," *Expert Systems with Applications*, vol. 169, p. 114338, 2021.

[18] X. Wang *et al.*, "Weakly supervised deep learning for whole slide lung cancer image analysis," *IEEE Trans. Cybernetics*, vol. 50, no. 9, pp. 3950–3962, 2019.

[19] A. Goode, B. Gilbert, J. Harkes, D. Jukic, and M. Satyanarayanan, "Openslide: A vendor-neutral software foundation for digital pathology," *Journal of Pathology Informatics*, vol. 4, 2013.

[20] G. Huang, Z. Liu, L. van der Maaten, and K. Q. Weinberger, "Densely connected convolutional networks," in *Proceedings of CVPR*, 2017.

[21] T. N. Kipf and M. Welling, "Semi-supervised classification with graph convolutional networks," in *ICLR Conference Track Proceedings*. OpenReview.net, 2017.

[22] T. Derr, Y. Ma, W. Fan, X. Liu, C. Aggarwal, and J. Tang, "Epidemic graph convolutional network," in *Proceedings of the 13th International Conference on Web Search and Data Mining*. New York, USA: Association for Computing Machinery, 2020, p. 160–168.

[23] K. Farahani *et al.*, "Computational Precision Medicine Radiology-Pathology challenge on Brain Tumor Classification 2020," Mar. 2020.

[24] A. Paszke *et al.*, "Pytorch: An imperative style, high-performance deep learning library," in *Advances in Neural Information Processing Systems*. Curran Associates, Inc., 2019, vol. 32, pp. 8024–8035.

[25] M. Fey and J. E. Lenssen, "Fast graph representation learning with PyTorch Geometric," in *ICLR Workshop on Representation Learning on Graphs and Manifolds*, 2019.

[26] M. McAvoy *et al.*, "Classification of glioblastoma versus primary central nervous system lymphoma using convolutional neural networks," *Scientific Reports*, vol. 11, no. 1, pp. 1–7, 2021.

[27] K. He, X. Zhang, S. Ren, and J. Sun, "Deep residual learning for image recognition," in *Proceedings of the IEEE conference on computer vision and pattern recognition*, 2016, pp. 770–778.

[28] A. Howard *et al.*, "Searching for mobilenetv3," in *Proceedings of the IEEE/CVF International Conference on Computer Vision*, 2019, pp. 1314–1324.

[29] X. Wang, S. Yang, and X. Wu, "Automatic glioma grading based on two-stage networks by integrating pathology and mri images," in *Brainlesion: Glioma, Multiple Sclerosis, Stroke and Traumatic Brain Injuries*. Springer International Publishing, 2021, pp. 455–464.